Research Square

Preprints are preliminary reports that have not undergone peer review.
They should not be considered conclusive, used to inform clinical practice,
or referenced by the media as validated information.

Separating local scale dependence from regional mixing in urban block-size distributions

Hiroyuki Shima

hshima@yamanashi.ac.jp

University of Yamanashi

Yuri Akiba

Mount Fuji Research Institute, Yamanashi Prefectural Government

Article

Keywords: urban blocks, heterogeneous mixtures, local exponent, scale dependence, urban morphology, statistical physics

Posted Date: September 10th, 2026

DOI: https://doi.org/10.21203/rs.3.rs-10848288/v1

License: This work is licensed under a Creative Commons Attribution 4.0 International License.
Read Full License

Additional Declarations: No competing interests reported.

Separating local scale dependence from regional mixing in urban block-size distributions

Hiroyuki Shima[1*] and Yuri Akiba[2]

[1*]Department of Environmental Sciences, University of Yamanashi, 4-4-37 Takeda, Kofu, 400-8510, Japan.

[2]Mount Fuji Research Institute, Yamanashi Prefectural Government, 5597-1 Kenmarubi, Kamiyoshida, Fujiyoshida, 403-0005, Japan.

*Corresponding author(s). E-mail(s): hshima@yamanashi.ac.jp;
Contributing authors: akiyuri@mfri.pref.yamanashi.jp;

Abstract

When data from heterogeneous regions are pooled, changing regional composition can mimic scale dependence absent within every region. We develop a workflow to distinguish this compositional effect from local change using urban block areas. At each area, the pooled local exponent is the size-conditioned mean of regional exponents, and its derivative equals mean within-region curvature minus a nonnegative heterogeneity penalty. Mixing exact power laws can only flatten the tail; steepening rules out composition alone and requires scale dependence in an active regional distribution or its support. For 116,184 blocks across Tokyo's 23 wards, common-support estimates identify lower-area within-ward steepening exceeding the penalty. At larger areas, mixing dominates, although the crossover is less stable. Synthetic controls recover null and positive curvature, and the lower-area sign survives whole-ward cluster resampling, block bootstrap, bandwidth and threshold changes, ward omission, alternative weights, and spline reconstruction. Larger areas shift weight toward wards with higher daytime/nighttime population ratios, but permutation evidence is suggestive rather than conclusive. All tested parametric families are rejected. The sign constraint, common-support estimation, mechanism exclusion, synthetic recovery, and Tokyo application provide a model-independent workflow for separating local structure from compositional mixing.

Keywords: urban blocks, heterogeneous mixtures, local exponent, scale dependence, urban morphology, statistical physics

1 Introduction

Measurements from heterogeneous urban regions are often pooled into a single city-wide distribution. This convenient aggregation creates an interpretive risk: the regions contributing most strongly can change with block size, making the pooled curve appear scale dependent even if each regional distribution is scale invariant. A bend in the aggregate therefore does not, by itself, identify a change in local urban structure.

Urban blocks and the streets that delimit them are elementary units of urban form. Their geometry reflects planarity, historical growth, spatial constraints, planning, and land use, and has consequently been studied through spatial-network and statistical-physics approaches [1–3]. Comparative road-network analysis has quantified how street geometry shapes travel across cities [4], while block- and neighbourhood-scale attributes have been connected to crime patterns and innovation vitality [5, 6]. These studies establish urban partitions as observable structures rather than merely cartographic units.

Urban morphology also acts across several spatial scales. Building–temperature associations can change with the size of the analysis unit [7], and within-city scaling can vary with heterogeneous spatial distributions and the balance of local and global interactions [8]. More generally, observed patterns and statistical conclusions can depend on observation scale, zoning, and aggregation context in heterogeneous social systems [9]. Scale dependence can therefore arise in two logically distinct ways: the local urban units may change with scale, or the composition of heterogeneous regions contributing to an aggregate may change.

Block-area distributions provide a direct setting in which to separate these effects. Broad block-size distributions have been described by Pareto, lognormal, gamma, and tempered forms [10–14]. In Tokyo, ward-level statistics have been related to block density, road width, and the ratio of daytime to nighttime population (RDN) [14, 15].

Akiba *et al.* previously used the present block-area and RDN observations to estimate one Pareto exponent per ward under ward-specific lower thresholds and to study its association with land use [15]. The present work asks a different question: it re-estimates all 23 conditional distributions under one common threshold and resolves their local curvature and changing mixture weights. None of the curvature, coarse-graining, synthetic-recovery, cluster-resampling, or held-out results reported here appeared in the earlier article.

At city scale, the 23 functionally distinct wards are pooled. A fitted citywide exponent therefore conflates the shape of each ward distribution with the changing fraction of the pooled density supplied by each ward.

Here we develop a scale-resolved, distribution-free diagnostic for this ambiguity. The contribution is an integrated inference workflow rather than an isolated algebraic identity. It combines an exact sign constraint, common-support nonparametric estimation, mechanism-class exclusion, synthetic recovery, ward-cluster uncertainty, and an empirical Tokyo test. The local exponent is the instantaneous negative slope of a log density, and its derivative with respect to logarithmic block area is termed curvature. We show that pooled curvature separates exactly into mean within-region curvature minus a nonnegative variance of regional local exponents. Mixing exact power laws can therefore only flatten; positive pooled curvature rules out a mixing-only explanation and requires scale dependence in at least one active regional distribution or its support. A companion covariance identity tracks how any region-level observable is sorted across block sizes. These relations connect established mixture-rate, covariance, and missing-information identities [16–18] in a common-support workflow for mechanism exclusion rather than selection.

Applying the framework to 116,184 blocks in Tokyo, we identify a robust lower-area interval in which within-ward steepening exceeds the heterogeneity penalty. The main estimate becomes heterogeneity dominated at larger areas, although this crossover

is less stable. We test the strong lower-area sign using resampling, smoothing and threshold changes, ward omission, alternative weights, and an independent density reconstruction. Parametric and held-out comparisons are used only to test over-specific descriptions; no unique microscopic process is inferred.

2 Results

2.1 Exact scale-resolved decomposition

Let A be block area and i index a region. On a common area range, let $f_i(A) > 0$ be the regional density and w_i its fixed sampling weight, with $\sum_i w_i = 1$. The pooled density is

$$f_{\mathrm{agg}}(A) = \sum_i w_i f_i(A), \tag{1}$$

and the fraction of that density supplied by region i at area A is

$$\rho_i(A) = \frac{w_i f_i(A)}{f_{\mathrm{agg}}(A)}. \tag{2}$$

Thus the relevant composition is size conditioned: even though w_i is fixed, $\rho_i(A)$ generally changes with A.

Define regional and pooled local exponents by

$$a_i(A) = -\frac{\mathrm{d}\ln f_i(A)}{\mathrm{d}\ln A}, \qquad a_{\mathrm{agg}}(A) = -\frac{\mathrm{d}\ln f_{\mathrm{agg}}(A)}{\mathrm{d}\ln A}. \tag{3}$$

Differentiating Eq. (1) gives the exact mean identity

$$a_{\mathrm{agg}}(A) = \sum_i \rho_i(A) a_i(A). \tag{4}$$

The pooled local exponent therefore lies within the contemporaneous range of regional exponents. More importantly, differentiating once more gives

$$\boxed{\frac{\mathrm{d}a_{\mathrm{agg}}}{\mathrm{d}\ln A} = \mathbb{E}_{\rho_A}\left[\frac{\mathrm{d}a_i}{\mathrm{d}\ln A}\right] - \mathrm{Var}_{\rho_A}[a_i(A)].} \tag{5}$$

Pooled curvature is the mean within-region curvature minus a heterogeneity penalty. The second term is nonnegative before subtraction, so regional variation in local exponents can only move pooled curvature toward flattening. The result also holds for a continuous mixture under standard differentiation conditions (Supplementary Information).

Regional composition has a parallel flow law. For any fixed region-level observable u_i,

$$\boxed{\frac{\mathrm{d}}{\mathrm{d}\ln A}\mathbb{E}_{\rho_A}[u_i] = -\,\mathrm{Cov}_{\rho_A}[u_i, a_i(A)].} \tag{6}$$

Regions with smaller local exponents have heavier local tails and become more represented as area increases. Equation (6) is a differential Price-type decomposition in the scale variable [17]; it describes compositional sorting and does not by itself imply causation.

Figure 1 summarizes the measurement and inference workflow. Two dimensionless quantities aid interpretation. Writing $W(A) = \mathbb{E}_{\rho_A}[\mathrm{d}a_i/\mathrm{d}\ln A]$ and $V(A) = \mathrm{Var}_{\rho_A}[a_i]$, the competition ratio is $\Xi = V/|W|$, while the bounded signed balance is

$$\mathcal{B}(A) = \frac{W(A) - V(A)}{|W(A)| + V(A)}. \tag{7}$$

For $W > 0$, $\Xi < 1$ or equivalently $\mathcal{B} > 0$ identifies within-region-dominated steepening; $\Xi > 1$ identifies heterogeneity-dominated flattening. For the sorting observable, $\eta_u = \mathrm{Corr}^2_{\rho_A}[u_i, a_i(A)]$ measures local alignment strength but not direction or causal importance.

2.2 Exclusion criterion and physical interpretation

If every active regional density is an exact power law on the same interval,

$$f_i(A) = c_i(A/A_*)^{-\alpha_i}, \qquad c_i > 0, \tag{8}$$

then each regional curvature is zero and Eq. (5) reduces to

$$\frac{\mathrm{d}a_{\mathrm{agg}}}{\mathrm{d}\ln A} = -\operatorname{Var}_{\rho_A}(\alpha_i) \le 0. \tag{9}$$

Positive mixing of exact powers can only flatten the pooled tail. Positive pooled curvature on a common support therefore excludes regional heterogeneity alone as a sufficient explanation. This is a local-exponent form of the classical decreasing-rate property of heterogeneous exponential mixtures [16]; under logarithmic area, a Pareto component becomes exponential.

One physical route to positive curvature is finite spatial extent or another large-area constraint. Writing

$$f_i(A) = c_i(A/A_*)^{-\alpha_i}T_i(A), \tag{10}$$

where $T_i(A) > 0$ suppresses large areas, define $\chi_i = -\mathrm{d}\ln T_i/\mathrm{d}\ln A$. The pooled distribution steepens only when

$$\mathbb{E}_{\rho_A}\left[\frac{\mathrm{d}\chi_i}{\mathrm{d}\ln A}\right] > \operatorname{Var}_{\rho_A}[\alpha_i + \chi_i(A)]. \tag{11}$$

Suppression is therefore not enough: its mean growth must exceed the heterogeneity penalty. Boundary, topographic, and multiscale constraints can alter urban-network morphology [19–21], but Eq. (11) does not select among them.

The decomposition is also consistent under nested coarse graining. If wards are first pooled into groups, the total variance splits into within-group and between-group parts

while citywide curvature remains unchanged. This permits an empirical partition into RDN strata without confusing a change of grouping with a change of the aggregate; the full derivation is in the Supplementary Information.

2.3 Tokyo block-area distributions

We analysed 116,184 positive block areas from Tokyo's 23 special wards together with one ward-level observable, RDN [15]. The largest ward-specific lower threshold, $A_* = 1850\,\mathrm{m}^2$, was imposed on every ward, leaving 51,055 blocks. All derivatives were evaluated on $5000 \le A \le 50000\,\mathrm{m}^2$. The common threshold is essential because Eq. (9) assumes a shared support; a changing support is itself a source of local scale dependence.

Figure 2 shows the main nonparametric reconstruction. With the prespecified central bandwidth 0.35, pooled curvature is positive from 5000 to approximately $1.74 \times 10^4\,\mathrm{m}^2$. Its 95% simultaneous bootstrap lower band remains positive to $1.03 \times 10^4\,\mathrm{m}^2$, and every bandwidth–leave-one-ward-out combination remains positive to $1.01 \times 10^4\,\mathrm{m}^2$. The lower-area steepening is therefore incompatible with a mixture of exact regional powers and requires within-ward scale dependence, potentially including finite-size or support effects.

The two terms of Eq. (5) locate the source of the sign. Near $10^4\,\mathrm{m}^2$, mean within-ward curvature is 0.394 and the local-exponent variance is 0.147, giving pooled curvature 0.246. Near $2 \times 10^4\,\mathrm{m}^2$, the corresponding values are 0.172 and 0.231, giving -0.0596. Thus within-ward steepening dominates at the lower scale, whereas heterogeneity dominates in the main estimate at the higher scale.

Synthetic recovery tests distinguish this lower-area signal from estimator artefacts (Supplementary Fig. S1). Five hundred datasets were generated with the observed ward counts and fitted Pareto baselines. Under exact-power components, the analytic

curvature near $10^4\,\mathrm{m}^2$ was -0.0237, and the reconstructed median and 95% simulation interval were -0.0253 and $[-0.155, 0.116]$. None of the 500 null estimates reached the empirical value 0.246 (one-sided Monte Carlo $p = 0.0020$). Under a prespecified tempered-power positive control, the analytic value was 0.300, the reconstructed median was 0.255 [0.107, 0.416], and all 500 estimates were positive.

The dimensionless diagnostics agree. Under empirical block-count weights, Ξ is 0.374 near $10^4\,\mathrm{m}^2$ and 1.347 near $2 \times 10^4\,\mathrm{m}^2$ [Fig. 4b]; the signed balances are 0.455 and -0.148. Grouping wards into low-, intermediate-, and high-RDN strata splits the variance as $0.101 + 0.0461 = 0.147$ at the lower scale and $0.122 + 0.1089 = 0.231$ at the higher scale. The between-stratum share rises from 31.3% to 47.1%, but regrouping leaves total curvature unchanged.

2.4 Regional sorting, robustness, and model checks

The size-conditioned mean RDN rises from 1.205 near $5000\,\mathrm{m}^2$ to 2.295 near $50000\,\mathrm{m}^2$ [Fig. 2d]. Larger observed blocks are therefore increasingly supplied by higher-RDN wards. The covariance in Eq. (6) reproduces the derivative of this shift; independent finite-difference and analytic-kernel evaluations differ by at most 1.36×10^{-4} across all bandwidth–ward-deletion cases (Fig. 3a,b). The local alignment η_R is 0.336 near $10^4\,\mathrm{m}^2$ and 0.308 near $2 \times 10^4\,\mathrm{m}^2$. However, 100,000 permutations of the 23 RDN labels give two-sided $p = 0.0608$ for the observed endpoint shift. The sorting is clear conditional on the observed labels but only suggestive under label exchangeability.

The lower-area sign is the stable result; the precise higher-area crossover is not. Across 69 bandwidth–leave-one-ward-out cases, $\mathcal{B}(10^4)$ ranges from 0.049 to 0.686, whereas $\mathcal{B}(2\times10^4)$ ranges from -0.892 to 0.147. Equal-ward and retained-area weights preserve positive balance at the lower scale and negative balance at the higher scale. An independent penalized-spline reconstruction [22, 23] remains positive to $1.63\times10^4\,\mathrm{m}^2$, with its first crossover between 1.51×10^4 and $1.64\times10^4\,\mathrm{m}^2$ across bin widths (Fig. 3c).

Four common thresholds reproduce the lower-area sign and the main-kernel crossover near $1.743 \times 10^4\,\mathrm{m}^2$ (Fig. 3d).

To relax block-level independence, 10,000 additional replicates resampled the 23 wards as intact clusters and retained every block in each selected ward (Supplementary Fig. S1). The pointwise 95% lower limit remained positive through $1.027 \times 10^4\,\mathrm{m}^2$, and the simultaneous lower limit remained positive through $9.152 \times 10^3\,\mathrm{m}^2$. Near $10^4\,\mathrm{m}^2$, the ward-cluster pointwise interval was [0.0185, 0.450], with 98.57% of replicates positive; the full-grid simultaneous interval included zero. Thus the lower-area conclusion is supported at the ward-cluster level, although its simultaneous range is shorter than under within-ward block resampling.

Pareto, cutoff-Pareto, stretched-exponential, and lognormal families were fitted on the same support. Every pooled family was rejected by a 1000-simulation Kolmogorov–Smirnov refit bootstrap (all $p = 0.0010$), although the lognormal had the lowest AIC and BIC. This distinction between relative ranking and absolute fit is important for finite-range broad tails [24, 25]. In 50 stratified 70/30 train–test splits, the lognormal best predicted conditional density and three of four derived features, whereas cutoff Pareto best predicted the RDN endpoint shift (Fig. 4c,d). No family was uniformly best. These checks do not reject finite-size suppression as a mechanism class; they show that the tested parametric realizations do not identify a unique process.

3 Discussion

The main result is a signed separation of effects that a single citywide exponent conflates. Mean within-ward curvature dominates at lower block areas, excluding exact-power mixing as a sufficient explanation. The main reconstruction reverses at larger areas, but bootstrap resampling and ward deletion support the lower-area regime more strongly than one exact crossover value. The scale-dependent effect is therefore localized rather than summarized by a global tail label.

This distinction complements quantitative urban-morphology research that separates local and global contributions to within-city scaling [8], tests scale-dependent morphology–temperature associations [7], or links block morphology to urban vitality [6]. Those analyses ask how measured form scales or predicts an external urban outcome. The present analysis asks a different prior question: when regional distributions are pooled, how much apparent scale dependence is generated by changing composition alone? Equation (5) answers this before a predictive morphology–outcome model is chosen. It can therefore be applied wherever administrative units, neighbourhoods, cities, or other conditions are aggregated.

Finite-size suppression, multiplicative processes, and network constraints can all supply the required positive regional term. Rejection of particular cutoff families does not reject the broader finite-size route; conversely, relative success of a lognormal approximation does not identify multiplication as the process [26, 27]. Direct street-network models illustrate the additional topology needed for a process-level test [28]. The present dataset contains block areas and ward labels but no block coordinates or adjacency, so the conclusion is a falsifiable mechanism-class constraint rather than microscopic identification (Fig. 5).

RDN probes a separate composition-flow identity. Larger blocks are more strongly represented by higher-RDN wards, but the permutation result and proxy status of RDN preclude a causal or order-parameter interpretation. Whole-ward resampling permits arbitrary dependence among blocks within each ward and supports the lower-area result, but block coordinates and adjacency are absent. We therefore cannot estimate distance-dependent autocorrelation or dependence across ward boundaries. Conclusions specific to Tokyo are consequently restricted to the 23 wards and common area range.

Within those limits, the framework provides a model-independent sequence of inference: reconstruct all conditional distributions on one support, calculate the

two curvature contributions, use their sign to exclude insufficient mixture explanations, and then evaluate candidate mechanisms with additional observables. This sequence separates evidence for local scale dependence from the stronger and presently unsupported claim of a unique urban-generative process.

4 Methods

4.1 Data provenance, relation to prior work, and common support

The block-area and ward-level RDN observations were first reported by Akiba *et al.* [15]. Vector White Map road data from the Geospatial Information Authority of Japan were imported into ArcGIS with Cartesian coordinates. Roads were binarized, road-enclosed polygons were recognized and converted to shapefiles, and polygon areas were calculated for all 23 special wards. RDN was calculated as daytime population divided by nighttime resident population using the 2015 census. The earlier article used ward-specific Pareto fits to study the association between one exponent per ward and RDN. The present analysis reuses the underlying area and RDN observations but does not reuse its fitted values as results; Fig. 2a is a new common-threshold re-estimation.

The full dataset contains 116,184 positive block areas. The 23 lower-tail thresholds reported with the earlier ward fits ranged up to $1850\,\mathrm{m}^2$; their maximum was applied to every ward here, retaining 51,055 observations on a common support. Ward weights in the main analysis were the retained block counts divided by the total retained count. Equal-ward and retained-area weights were analysed as alternatives. Derivative-based results were restricted to 5000–$50000\,\mathrm{m}^2$ to avoid threshold-boundary and sparse-tail instabilities.

4.2 Nonparametric reconstruction

For $\ell = \ln(A/A_*)$, each ward density $q_i(\ell)$ was reconstructed with a reflected Gaussian kernel density estimator. Because $f_i(A) = q_i(\ell)/A$,

$$a_i(A) = 1 - \frac{q_i'(\ell)}{q_i(\ell)}. \tag{12}$$

Analytic first and second kernel derivatives were evaluated on a 260-point geometric grid. The central bandwidth was 0.35; 0.30 and 0.40 were sensitivity values. The aggregate density, size-conditioned weights, local exponents, curvatures, balance, and RDN sorting were then calculated directly from Eqs. (1)–(7). A penalized log-spline reconstruction with generalized cross-validation supplied an estimator-independent check [22, 23].

4.3 Synthetic recovery

Synthetic samples retained the 23 observed ward counts, common threshold, 260-point grid, and bandwidth 0.35. The exact-power null used exponential log-area components with rates equal to the 23 fitted Pareto baselines minus one. The positive control multiplied every component by $\exp[-\eta(A/A_* - 1)]$, with the prespecified dimensionless value $\eta = 0.06$; its analytic local curvature is $\eta A/A_*$. For each scenario, 500 independently generated datasets were reconstructed by the same reflected-kernel procedure as the observations. We compared reconstructed and analytic curvature at 10^4 and $2 \times 10^4\,\mathrm{m}^2$, recorded sign recovery and curve error, and compared the Tokyo value with the exact-power null by the finite-simulation one-sided $p = (b + 1)/(R + 1)$. Full curves and numerical summaries are provided in the Supplementary Information.

4.4 Uncertainty, spatial dependence, and robustness

Five hundred stratified bootstrap replicates resampled blocks within wards while retaining ward counts. Pointwise intervals were obtained from replicate quantiles; the aggregate-curvature band was calibrated simultaneously across the displayed grid. Because the block-level procedure assumes exchangeability within wards, a second bootstrap resampled the 23 wards with replacement as intact clusters for 10,000 replicates. All blocks and the reconstructed conditional density of a selected ward moved together, permitting arbitrary within-ward dependence. Pointwise quantiles and a maximum-studentized simultaneous band were computed over the same grid. This cluster procedure cannot adjust dependence across ward boundaries because block coordinates and adjacency are unavailable.

Robustness analyses combined three bandwidths with deletion of each ward, tested four common lower thresholds, compared three weighting schemes, and divided wards into two to four RDN strata.

The RDN sorting identity was audited through independent analytic-kernel and finite-difference calculations. Its inferential label test used 100,000 random permutations of the 23 fixed RDN values. The permutation p-value is descriptive under label exchangeability and is not a causal test.

4.5 Parametric and held-out comparisons

Pareto, cutoff-Pareto, stretched-exponential, and lognormal families were fitted on the common support. Absolute pooled fit was evaluated by a 1000-simulation Kolmogorov–Smirnov bootstrap in which each simulated dataset was refitted. Predictive comparisons used 50 prespecified stratified splits, independently holding out 30% of observations in every ward. Models were fitted only to training data and evaluated

on held-out log predictive density, curvature, crossover, the RDN curve, and its endpoint shift. Complete numerical protocols, identity audits, and comparison tables are provided in the Supplementary Information.

Data availability

The processed block-area and ward-level RDN data supporting the findings of this study are available from the corresponding author upon reasonable request.

Code availability

The custom Python code, fixed random seeds, and complete numerical outputs required to reproduce the analyses and figures are available from the corresponding author upon reasonable request and will be supplied to editors and referees during peer review.

References

[1] Cardillo, A., Scellato, S., Latora, V. & Porta, S. Structural properties of planar graphs of urban street patterns. *Phys. Rev. E* **73**, 066107 (2006).

[2] Barthélemy, M. Spatial networks. *Phys. Rep.* **499**, 1–101 (2011).

[3] Strano, E., Nicosia, V., Latora, V., Porta, S. & Barthélemy, M. Elementary processes governing the evolution of road networks. *Sci. Rep.* **2**, 296 (2012).

[4] Maia, G. *et al.* A global empirical study on how street networks facilitate driving longer distances. *Sci. Rep.* **13**, 18154 (2023).

[5] De Nadai, M. *et al.* Socio-economic, built environment, and mobility conditions associated with crime: A study of multiple cities. *Sci. Rep.* **10**, 13871 (2020).

[6] Ruan, Y., Zhang, X., Wang, J. *et al.* Understanding the role of urban block morphology in innovation vitality through explainable machine learning. *Sci. Rep.* **15**, 21337 (2025).

[7] Han, W. Analyzing the scale dependent effect of urban building morphology on land surface temperature using random forest algorithm. *Sci. Rep.* **13**, 19312 (2023).

[8] Dong, L., Huang, Z., Zhang, J. & Liu, Y. Understanding the mesoscopic scaling patterns within cities. *Sci. Rep.* **10**, 21201 (2020).

[9] Balsa-Barreiro, J., Menendez, M. & Morales, A. J. Scale, context, and heterogeneity: the complexity of the social space. *Sci. Rep.* **12**, 9037 (2022).

[10] Lämmer, S., Gehlsen, B. & Helbing, D. Scaling laws in the spatial structure of urban road networks. *Physica A* **363**, 89–95 (2006).

[11] Fiałkowski, M. & Bitner, A. Universal rules for fragmentation of land by humans. *Landscape Ecol.* **23**, 1013–1022 (2008).

[12] Bitner, A., Hołyst, R. & Fiałkowski, M. From complex structures to complex processes: Percolation theory applied to the formation of a city. *Phys. Rev. E* **80**, 037102 (2009).

[13] Riascos, A. P. Universal scaling of the distribution of land in urban areas. *Phys. Rev. E* **96**, 032302 (2017).

[14] Usui, H. & Asami, Y. Size distribution of urban blocks in the tokyo metropolitan region: Estimation by urban block density and road width on the basis of normative plane tessellation. *Int. J. Geogr. Inf. Sci.* **32**, 120–139 (2018).

[15] Akiba, Y., Wang, S., Sato, M. & Shima, H. Impact of land-use differences on block-size distribution in tokyo. *J. Phys. Soc. Jpn.* **92**, 104801 (2023).

[16] Proschan, F. Theoretical explanation of observed decreasing failure rate. *Technometrics* **5**, 375–383 (1963).

[17] Price, G. R. Selection and covariance. *Nature* **227**, 520–521 (1970).

[18] Louis, T. A. Finding the observed information matrix when using the EM algorithm. *J. R. Stat. Soc. Ser. B* **44**, 226–233 (1982).

[19] Murcio, R., Masucci, A. P., Arcaute, E. & Batty, M. Multifractal to monofractal evolution of the london street network. *Phys. Rev. E* **92**, 062130 (2015).

[20] Barthélemy, M., Boeing, G., Chiaradia, A. & Webster, C. J. Surfacic networks. *PNAS Nexus* **4**, pgae585 (2025).

[21] Gu, X., Wang, H., Lyu, J., Zhang, M. & Ge, Q. Exploring the impacts of topography on characteristics of urban road network: A global empirical analysis. *Cities* **160**, 105848 (2025).

[22] Silverman, B. W. On the estimation of a probability density function by the maximum penalized likelihood method. *Ann. Stat.* **10**, 795–810 (1982).

[23] Kooperberg, C. & Stone, C. J. A study of logspline density estimation. *Comput. Stat. Data Anal.* **12**, 327–347 (1991).

[24] Clauset, A., Shalizi, C. R. & Newman, M. E. J. Power-law distributions in empirical data. *SIAM Rev.* **51**, 661–703 (2009).

[25] Malevergne, Y., Pisarenko, V. & Sornette, D. Testing the pareto against the lognormal distributions with the uniformly most powerful unbiased test applied

to the distribution of cities. *Phys. Rev. E* **83**, 036111 (2011).

[26] Sornette, D. Multiplicative processes and power laws. *Phys. Rev. E* **57**, 4811–4813 (1998).

[27] Mitzenmacher, M. A brief history of generative models for power law and lognormal distributions. *Internet Math.* **1**, 226–251 (2004).

[28] Barthélemy, M. & Boeing, G. Universal model of urban street networks. *Phys. Rev. Lett.* **135**, 137401 (2025).

Acknowledgements

We thank Prof. Motohiro Sato for fruitful discussions. This work was supported by the Obayashi Foundation and JSPS KAKENHI Grant Nos. JP24K01111 and JP24K17370.

Author contributions

H.S.: Conceptualization, Methodology, Formal analysis, Writing—original draft, and Writing—review and editing. Y.A.: Conceptualization, Formal analysis, and Writing—review and editing. Both authors approved the submitted version.

Additional information

Competing interests: The authors declare no competing interests.

Supplementary information: Supplementary Information accompanies this paper.

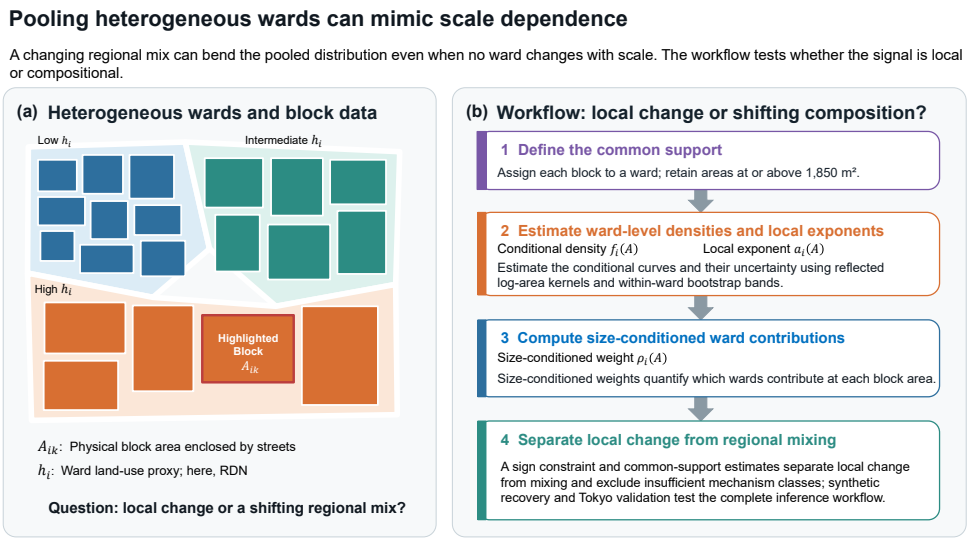


Fig. 1 Pooling risk and integrated inference workflow. (a) Streets partition an urban region into blocks with measured areas A_{ik}. The index i identifies a ward, while h_i denotes a ward-level observable, represented by RDN in the Tokyo analysis. Because ward contributions can change with block area, pooling can mimic scale dependence even when every ward-level tail is scale invariant. Colours and polygons are schematic and encode no measured geography. (b) Common-support reconstruction, size-conditioned weights, the exact sign constraint, mechanism-class exclusion, synthetic recovery, and the Tokyo test distinguish local change from compositional mixing without assuming a parametric tail family.

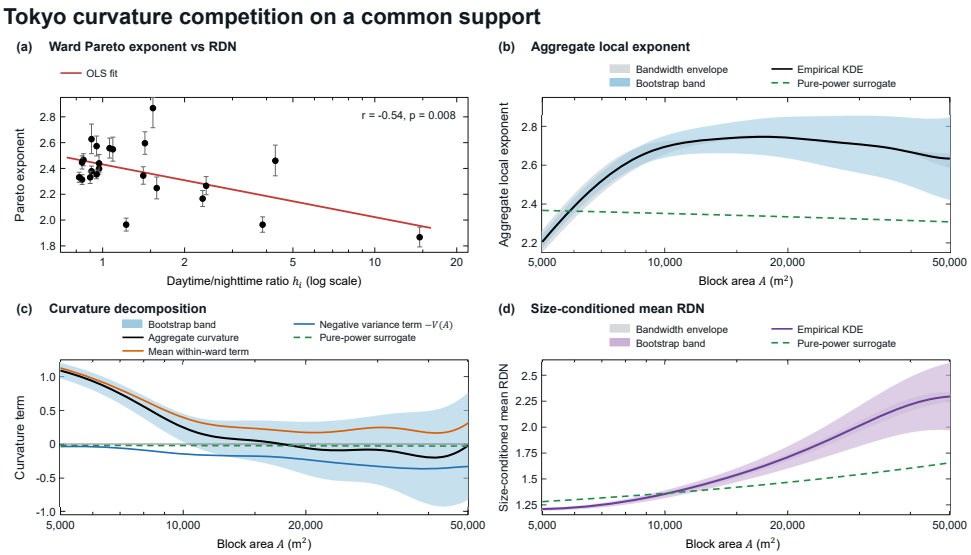


Fig. 2 Empirical curvature competition on the common support. (a) Ward Pareto exponents versus RDN, newly re-estimated at the present common threshold rather than copied from the earlier ward-specific analysis; vertical bars are model-based 95% confidence intervals. (b) Pooled local exponent from the empirical kernel reconstruction and fitted pure-power surrogate. (c) Exact decomposition of pooled curvature into the mean within-ward contribution and negative size-conditioned local-exponent variance, with a simultaneous bootstrap band. (d) Size-conditioned mean RDN versus block area. Grey envelopes span the three kernel bandwidths.

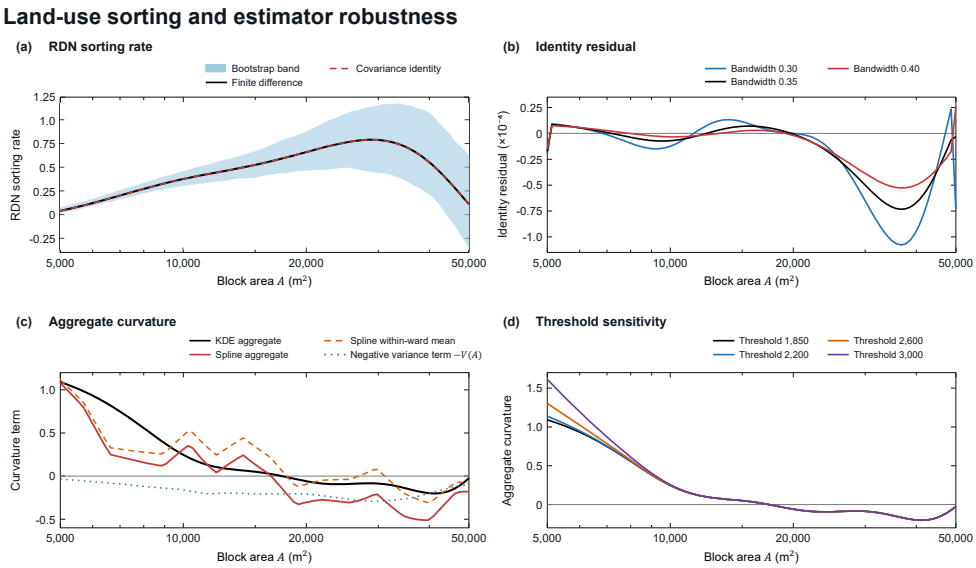


Fig. 3 Land-use sorting and robustness checks. (a) Finite-difference rate of change of the size-conditioned mean RDN and the independently assembled negative covariance, with pointwise stratified-bootstrap uncertainty. (b) Numerical residual of the sorting identity for three bandwidths. (c) Pooled curvature from kernel and independent penalized-spline reconstructions, with the spline within-ward and negative-variance contributions. (d) Pooled curvature for four common lower thresholds. The robust comparison is the initial positive-curvature regime and its first crossover.

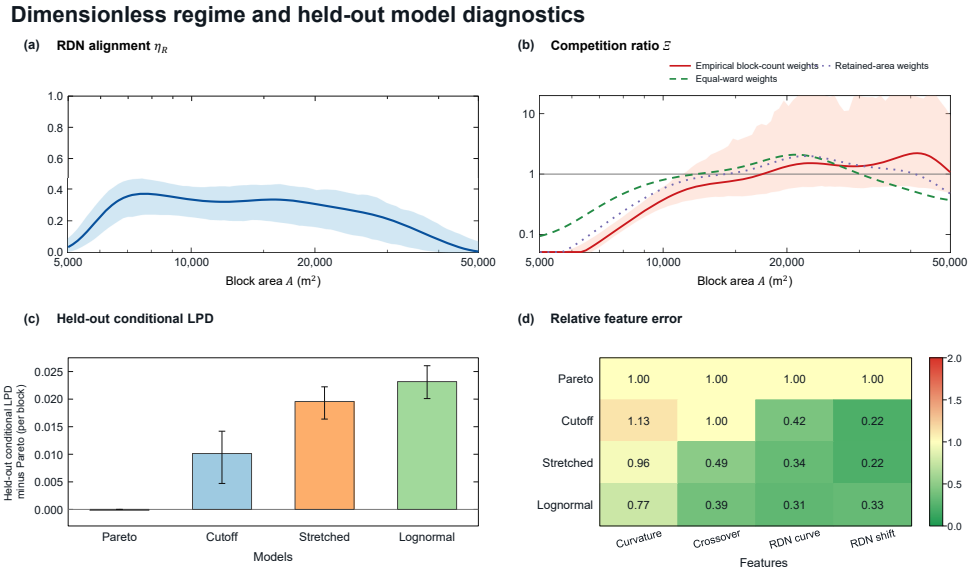


Fig. 4 Dimensionless regime and held-out model diagnostics. (a) Squared size-conditioned RDN–local-exponent alignment η_R, with a pointwise 95% bootstrap band. (b) Competition ratio Ξ for empirical block-count weights and two alternative schemes; the shaded region is the pointwise 95% bootstrap band for empirical weights. (c) Paired held-out conditional log predictive density relative to Pareto over 50 splits. (d) Median feature errors relative to the Pareto median. Lognormal minimizes the first three feature errors, whereas cutoff Pareto minimizes endpoint-shift error; no family is uniformly best.

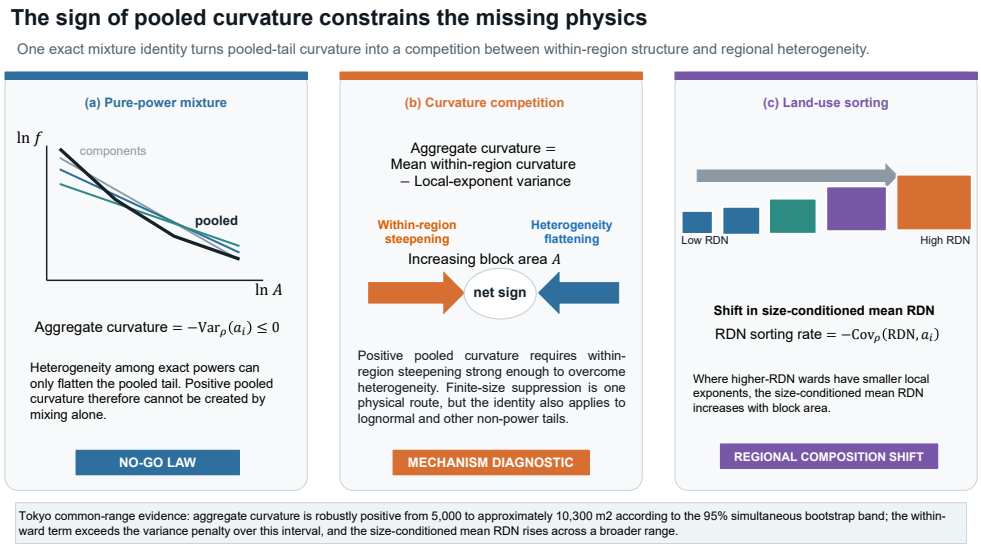


Fig. 5 Mechanism map for the aggregation-first diagnosis. Pure-power regional heterogeneity contributes only the negative local-exponent variance and cannot create positive pooled curvature. General curvature separates mean within-region curvature from this heterogeneity penalty, while the size-conditioned covariance controls sorting of a region-level observable. The bottom band summarizes the common-support Tokyo result.

Supplementary Files

This is a list of supplementary files associated with this preprint. Click to download.

- CityBlockSciRepsupple.pdf